



ALMA MATER STUDIORUM
UNIVERSITÀ DI BOLOGNA

ARCHIVIO ISTITUZIONALE
DELLA RICERCA

Alma Mater Studiorum Università di Bologna Archivio istituzionale della ricerca

Reprint of: In-field and non-destructive monitoring of grapes maturity by hyperspectral imaging

This is the final peer-reviewed author's accepted manuscript (postprint) of the following publication:

Published Version:

Benelli, A., Cevoli, C., Ragni, L., Fabbri, A. (2022). Reprint of: In-field and non-destructive monitoring of grapes maturity by hyperspectral imaging. BIOSYSTEMS ENGINEERING, 223, Part B(November 2022), 200-208 [10.1016/j.biosystemseng.2022.10.003].

Availability:

This version is available at: <https://hdl.handle.net/11585/1002423> since: 2025-01-20

Published:

DOI: <http://doi.org/10.1016/j.biosystemseng.2022.10.003>

Terms of use:

Some rights reserved. The terms and conditions for the reuse of this version of the manuscript are specified in the publishing policy. For all terms of use and more information see the publisher's website.

This item was downloaded from IRIS Università di Bologna (<https://cris.unibo.it/>).
When citing, please refer to the published version.

(Article begins on next page)

1 **In-field and non-destructive monitoring of grapes maturity by hyperspectral imaging**

2

3 Alessandro Benelli^a, Chiara Cevoli^{a,b*}, Luigi Ragni^{a,b}, Angelo Fabbri^{a,b}

4

5 ^a*Department of Agricultural and Food Sciences, Alma Mater Studiorum, University of Bologna, Piazza Goidanich 60,*
6 *Cesena, 47521, Italy*

7 ^b*Interdepartmental Centre for Agri-Food Industrial Research, Alma Mater Studiorum, University of Bologna, Via Quinto*
8 *Bucci 336, Cesena, 47521, Italy*

9 **Corresponding author: chiara.cevoli3@unibo.it*

10

11 **Abstract**

12

13 Monitoring the quality attributes of grapes is a practice that allows the state of ripeness to be checked
14 and the optimal harvest time to be identified. A non-destructive method based on hyperspectral
15 imaging (HSI) technology was developed. Analyses were carried out directly in the field on a
16 ‘Sangiovese’ (*Vitis vinifera* L.) vineyard destined for wine production, by using a Vis/NIR (400–
17 1000 nm) hyperspectral camera. One vineyard row was analysed on 13 different days during the pre-
18 harvest and harvest time. The soluble solids content (SSC) expressed in terms of °Brix was measured
19 by a portable digital refractometer. Afterwards, the grape samples were split in two classes: the first
20 one composed by the samples characterised by a °Brix lower than 20 (not-ripe), while the second one
21 by the samples with a °Brix higher than 20 (ripe). Grape mean spectra were extracted from each
22 hyperspectral image and used to predict the SSC by partial least squares regression (PLS), and to
23 classify the samples into the two classes by PLS discriminant analysis (PLS-DA). SSC was predicted
24 with a $R^2=0.77$ (RMSECV=0.79 °Brix), and the samples were correctly classified with a percentage
25 from 86 to 91%. Even if the number of wavelengths was limited, the percentages of correctly
26 classified samples were again within the above-mentioned range. The present study shows the

27 potential of the use of HSI technology directly in the field by proximal measurements under natural
28 light conditions for the prediction of the harvest time of the ‘Sangiovese’ red grape.

29
30 **Keywords:** hyperspectral, in-field, grape, wine, harvest, classification

31

32

33 **1. Introduction**

34 Italy is the largest wine producer in the world, with a production in 2018 of 5,480 million litres
35 (18.8% of world production) (OIV International Organisation of Vine and Wine, 2019). In an
36 industrialised wine growing system, monitoring the quality attributes, such as soluble solids content
37 (SSC), acidity and anthocyanin content of grapes is extremely important: well-planned monitoring
38 allows to check the growth and ripening of the grapes, and finally to decide when to proceed with the
39 harvest (Delrot, Medrano, Or, Bavaresco, Grando, 2010). For instance, by managing irrigation
40 through the use of techniques such as the regulated deficit irrigation, significant increases in SSC and
41 anthocyanins can be achieved which together with a decrease in yield and berry size can lead to
42 substantial improvements in grape quality (Acevedo-Opazo, Ortega-Farias, Fuentes, 2010;
43 Pellegrino, Lebon, Simonneau, Wery, 2005).

44 Monitoring of grape quality attributes can be carried out directly in the field using traditional
45 destructive techniques. Alternatively, quality attributes can be estimated by non-destructive
46 techniques, such as near-infrared (NIR) spectroscopy. Portable NIR instruments were used to
47 determine the following quality attributes of grapes: water content, SSC, reductant sugars, pH,
48 titratable acidity, maturity index (sugar/acidity ratio), extractable anthocyanins, potential
49 anthocyanins (Teixeira Dos Santos, Lopo, Páscoa, Lopes, 2013).

50 Over the last two decades the use of HSI technology in the quality assessment of fruits and vegetables
51 has become of increasing interest (Chandrasekaran, Panigrahi, Ravikanth, Singh, 2019; Liu, Zeng,
52 Sun, 2015). HSI was initially limited to controlled environments such as laboratories but gradually,

53 thanks to the miniaturisation and improved computing and data storage capabilities, it began to be
54 used directly in the field (Benelli, Cevoli, Fabbri, 2020). Hyperspectral images can be captured either
55 remotely by airborne vehicles and unmanned aerial vehicles (Ishida et al., 2018; Matese & Di
56 Gennaro, 2015; Zarco-Tejada et al., 2013) or by ground vehicles (Deery, Jimenez-Berni, Jones,
57 Sirault, Furbank, 2014; Gutiérrez, Fernández-Navales, Diago, Tardaguila, 2018a; Huang, Lee,
58 Thomson, Reddy, 2016; Jay et al., 2017; Underwood, Wendel, Schofield, McMurray, Kimber, 2017;
59 Wendel, Underwood, Walsh, 2018; Whetton, Waine, Mouazen, 2018), which produces proximal
60 hyperspectral images with high spatial resolution. Proximal HSI could therefore allow non-
61 destructive, contactless, and automated monitoring of grape quality attributes. Moreover, the
62 acquisition of hyperspectral images can be performed continuously, enabling the rapid scanning of
63 large areas. Hyperspectral data is characterised by two spatial and one spectral dimension, therefore
64 only specific regions of interest (ROIs) can be selected, and the residual regions can be excluded. In
65 this sense, hyperspectral analysis is useful to guide the choice of true multispectral less expensive
66 solutions.

67 Concerning in-field grape studies, Gutiérrez et al. (2018a) adopted an on-the-go HSI system for the
68 classification of 30 grapevine varieties directly acquired in the field. Through the development of
69 classification models based on support vector machines (SVM) and multilayer perceptron (MLP),
70 prediction performance (F1 score) up to 0.99 was achieved. The same on-the-go HSI system
71 described above, combined with SVM, was adopted to estimate SSC and anthocyanin concentration
72 of wine grapes (Gutiérrez et al., 2018b). Determination coefficients (R^2) of 0.92 (RMSE=1.274 °Brix)
73 and 0.83 (RMSE=0.211 mg g⁻¹) were obtained for the prediction of SSC and anthocyanin
74 concentration, respectively. These two studies highlight the potential of HSI to monitor the indices
75 of grape ripening directly in the field and therefore to improve vineyard decisions and management.
76 Non-linear statistical methods were used in both studies. Considering the results just mentioned, it
77 would be interesting to investigate whether, even combining HSI with linear methods and reducing
78 the number of wavelengths, it is possible to monitor the degree of grape maturity directly in the field.

79 Furthermore, considering a possible application of this technique, a simple binary model able to
80 simply determine whether grapes are ripe for harvesting could be interesting.

81 Thus, the present study aims to identify the proper degree of ripeness, suitable for harvesting wine
82 grapes, through the observation of the SSC evolution by means of HSI technology applied directly in
83 the field. The mean spectra were extracted from each hyperspectral image and used to predict the
84 SSC and to classify the samples into the two classes (not-ripe and ripe), by partial least squares
85 regression (PLS) and discriminant analysis (PLS-DA), respectively.

86

87 **2. Materials and methods**

88 *2.1 Samples*

89 One side of a row of ‘Sangiovese’ (*Vitis vinifera* L.) grape vineyards, located near Cesena, Italy, was
90 analysed on 13 different days in the period between August 20th and October 4th, 2019 (from pre-
91 harvest to harvest time). The row was divided into 11 sections; from each section 3, grapes were taken
92 for each day of analysis, for a total of 429 samples.

93

94 *2.2 Hyperspectral acquisitions*

95 The adopted push-broom hyperspectral camera (Nano-Hyperspec VNIR, Headwall Photonics, Inc.,
96 Fitchburg, MA, USA) scans single lines in a sequence, each one consisting of 640 voxels: the image
97 is created by moving the camera along the scanning direction (Fig. 1a). Each voxel contains, in
98 addition to the two spatial dimensions, a Vis/NIR spectrum (400–1000 nm) characterized by 272
99 spectral bands, with a nominal spectral resolution of 2.2 nm. The mounted lens has an effective focal
100 length of 17 mm, with the optical axis perpendicular to the side of the vineyard row (scanned surface)
101 analysed (Figure 1b). The camera was installed on a garden cart (Fig. 1b) 120 cm above the ground
102 and it was powered by a 12 V, 45 Ah automotive battery through a DC to AC power inverter. The
103 scans were performed at about 1.6 m from the side of the vineyard row.

104 Direct sunlight with clear sky conditions, was used as a light source. To reduce the fluctuation of the
105 sample temperature, all the acquisitions were carried during the same period of the day, from
106 10:30 a.m. to 12:00 p.m.

107 The frame rate was set to approximately 100 frames s⁻¹. The exposure time was set from 6 to 8 ms,
108 depending on the light intensity, and was achieved through calibration, by framing a white high-
109 reflectance matter panel, placed at the same distance as the vineyard row, to cover the entire angle of
110 view of the camera. Given the clear sky conditions and the short time required, about 10 min,
111 acquisition of hyperspectral images of the 11 vineyard row sections and calibration was carried out
112 only once per day.

113 The raw diffuse reflectance spectrum (R_R) was extracted from the HS images. The calibrated diffuse
114 reflection spectrum (R_C) was calculated by applying the following equation:(Guo et al., 2019):

$$115 \quad R_C = \frac{R_R - R_D}{R_W - R_D} \quad (1)$$

116 where R_D is the reflectance spectrum of dark reference, obtained by applying the cap on the lens; R_W
117 is the reflectance spectrum of white reference, obtained by means calibration with the white high-
118 reflectance matte panel reported above.

119 A hyperspectral image from each of the 11 sections obtained from the vineyard row, was acquired
120 per day of analysis (Fig. 1c): therefore, during the 13 d of analysis, a total of 143 vineyard row sections
121 were scanned.

122

123 *2.3 Soluble solids content measurement*

124 After the acquisition of the images, the SSC, expressed in °Brix, was measured on 3 grape berries
125 (randomly selected) from each of the 11 sections by using a portable digital refractometer (PR-101
126 Digital Refractometer, ATAGO CO., LTD, Tokyo, Japan). Subsequently, the mean for each section
127 was calculated.

128 One-way analysis of variance (ANOVA) with Tukey-HSD post-hoc test (p-level < 0.05) was applied
129 to evaluate significant differences between SSC means over the different days of analysis.

130 *2.4 Hyperspectral images elaboration*

131 ROI selection was made using the software HyperCube, v. 11.52 (U.S. Army Engineer Research and
132 Development Center (ERDC), USA). For each image, 5 points and a maximum of a further 120
133 adjacent points (11 x 11 voxels matrix, with the selected point in the centre of the matrix) were
134 selected on 5 different berries directly illuminated by the sun, not in the shade. The (reference) points
135 included in the classification were characterized by a metric distance from the mean (signature)
136 spectrum of the manually selected points within the range (tolerance threshold) [0,0.04] (Fig. 2). The
137 metric distance was calculated by applying the absolute difference (Manhattan) function (Eq. (2))
138 (Deborah, Richard, Hardeberg, 2015) and normalised in the range [0,1].

139
$$d(R_1, R_2) = \sum_{\lambda} |R_{1,\lambda} - R_2| \quad (2)$$

140 where R_1, R_2 are two reflectance spectra.

141 From the spectra of the classified points, the mean spectrum for each hyperspectral image was
142 calculated.

143 The spectral bands between 400–424 nm were omitted as a result of the low signal-to-noise ratio
144 produced by the sensor, as reported in Wendel et al. (2018). The spectra were smoothed (Savitzky-
145 Golay method; polynomial order: 2; smoothing points: 15) to reduce noise from the spectra and
146 following pre-treated by the standard normal variate (SNV) method, first derivative (D1) and finally
147 mean centred (MC). The SNV is one of the most common pre-processing method used to correct
148 spectra for changes in optical path length and light scattering, while the derivatives have the capability
149 to remove both additive and multiplicative effects in the spectra (Rinnan, van den Berg, Engelsen,
150 2009). After SNV, each spectrum will have a mean of 0 and a standard deviation of 1.

151 Principal component analysis (PCA) was applied to the mean spectra as exploratory technique to
152 visualize the data according to °Brix and time evolution. Subsequently, a preliminary PLS regression
153 model was built to estimate the SSC. The validation was carried out by the venetian blind cross-
154 validation method (segments: 10).

155 PLS-DA models were built to classify the samples according to °Brix. In particular, classification
156 models with 2 categories (not-ripe and ripe) were developed: according to Bucelli, Costantini and
157 Storchi (2010), the first class was composed by the samples characterized by a °Brix lower than 20
158 (0), while the second one by the samples with a °Brix equal or higher than 20 (1).

159 The sample dataset (n = 143) was split in calibration (venetian blinds cross-validation, including 75%
160 of the samples) and external validation set (25% of the samples) by using the Onion method
161 (Gallagher et al., 2004). The threshold value, able to identify the belonging category of each sample
162 into one of the groups, was defined by using a probabilistic approach based on Bayes's rule. To avoid
163 the model over-fitting, the optimal number of latent variables were chosen by plotting the root mean
164 square error of cross-validation (RMSECV) as a function of the number of components and by
165 identifying where the curve reaches a local minimum. The receiver operating characteristic (ROC)
166 curves in prediction were evaluated to assess the goodness of the models.

167 All the chemometrics models were developed by using PLS Toolbox for Matlab2018a.

168

169 **3. Results and discussion**

170 Means and standard deviation of the °Brix measured during the 13 d of analysis are reported in Table
171 1. The increase between the first and last day was of 27.5%, from 17.8 °Brix (day I) to 22.7 °Brix
172 (day XIII). Several significant differences between the °Brix mean values were achieved over the
173 different days of analysis. The whole data set was characterized by a mean value of 20.6 ± 1.7 °Brix,
174 which make suitable to split it in two subsets with a threshold of 20 °Brix.

175 Raw and pre-treated (smoothing and SNV) mean spectra of all the samples by day of analysis are
176 presented in Fig. 3. In the Vis/NIR region (400–1000 nm), the visible spectrum (400–700 nm)
177 presents the absorption bands of some substances used as ripening indexes of fruit: anthocyanins at
178 around 500 nm, carotenoids at 570–590 nm, and chlorophyll *a* at 680–710 nm (ElMasry, Wang,
179 ElSayed, Ngadi, 2007; Munera et al., 2017). In the NIR region (700–1000 nm), absorption bands of
180 water at 760 nm and 960–970 nm are characterised by the overtone of O-H bonds (McGlone &

181 Kawano, 1998; Nicolaï et al., 2007): since the water content of a ripe wine grape is 70–80% (FAO
182 Food and Agriculture Organization, 2009), it can be expected that the water related absorption band
183 will prevail. Absorption band around 840 nm was associated with sugar (Pu, Liu, Wang, Sun, 2016);
184 moreover, peaks observed in the 950–1000 nm region were related to both water and carbohydrates,
185 as the second overtone of O-H and N-H, a combination band of O-H bonds and the third overtone of
186 C-H, were found in the region (Camps & Christen, 2009). As observed, the water absorption peaks
187 in the NIR (700–1000 nm) spectral region are not very marked and wide. Therefore, spectral
188 information from SSC in the 800–1000 nm range will tend to be less covered by water (Camps &
189 Christen, 2009; Manley, Joubert, Myburgh, Kidd, 2007).

190 The score plot of the first two principal components (PC1: 59%; PC2: 28%) resulting from PCA
191 shows the samples distribution according to the day of analysis. A tendency to place the samples from
192 left to right can be observed on PC1, starting from day I (quadrant III) to day XIII (quadrant IV)
193 (Figure 4a).

194 A similar distribution can be observed according to the SSC: the samples are distributed along PC1,
195 mainly on the left those with $SSC < 20$ °Brix (quadrants II and III), on the right those with
196 $SSC \geq 22$ °Brix (quadrants I and IV) (Fig. 4b).

197 The best PLS results were obtained pre-treating the spectra by SNV + MC. Particularly, $R^2 = 0.768$
198 and $RMSECV = 0.79$ °Brix were achieved in cross-validation with 7 latent variables. Figure 5 shows
199 the predicted versus measured °Brix values.

200 These results agree with those present in literature and developed by using spectra in the same
201 wavelength range and acquired directly in-field. Furthermore, regardless of the R^2 values, the RMSE
202 is substantially lower. Diezma-Iglesias, Barreiro, Blanco and García-Ramos (2008) predicted SSC on
203 480 samples of ‘Cabernet Sauvignon’ by using a portable hand-held spectrometer (590–1090 nm),
204 reporting a $R^2 = 0.72$, while Guidetti, Beghi and Bodria (2010) working with a simple Vis/NIR system
205 in the range from 400 to 1000 nm, obtained in prediction $r=0.82$ ($R^2=0.67$) and $RMSEP=1.48$ °Brix.
206 Gutiérrez et al. (2018b) used the HSI technique (400–1000 nm) to measure SSC in wine grapes in

207 real time. R^2 of 0.91 (RMSE = 1.358 °Brix) and 0.92 (RMSE = 1.274 °Brix) were achieved in cross
208 validation and prediction, respectively, by using the SVM techniques.

209 PLS-DA results, in terms of percentage of correctly classified samples, are reported in Table 2. The
210 percentages ranged from 86 to 91%. Considering the prediction set, the best result was obtained
211 applying as pre-treatment the SNV + MC. The results obtained with the hyperspectral technique
212 improved those achieved by Guidetti et al. (2010) by using of a portable contact system. The authors
213 combined Vis/NIR spectroscopy in the wavelength range 450 – 980 nm with PLS-DA to classify
214 grape samples in two groups based on SSC (threshold = 21 °Brix), obtaining a percentage of samples
215 correctly classified (in prediction) of 77.1% (Guidetti et al., 2010).

216 The ROC curves in prediction (Fig. 6) summarise the trade-off between specificity (number of
217 samples predicted to not be in the class divided by the actual number not in the class) and sensitivity
218 (number of samples predicted to be in the class divided by number actually in the class) for the PLS-
219 DA classification models. The area under the curves (AUC = 0.9855 for SNV + MC and
220 AUC = 0.9578 for SNV + D1 + MC) suggest that the models were characterised by a high degree of
221 discrimination, confirming that the best model was those developed considering only the SNV + MC
222 as pre-treatment.

223 Results, in terms of probability (Bayes's rule) of belonging to the class °Brix < 20, are shown in Fig.
224 7. The higher a sample is placed, the higher the probability that it will be classified as a member of
225 the °Brix < 20 class. Consequently, samples classified as members of the other class (°Brix \geq 20)
226 are placed at the bottom of the graph. The threshold value (dotted red line) was set at 0.5 (probability
227 of 50%); samples with a probability lower than this value are considered improperly classified.

228 Considering the SNV + MC and SNV + D1 + MC pre-treatments, 89% and 77% of the samples (in
229 prediction) were classified with a probability higher than 70%.

230 Figure 8 shows the VIP (variable importance in projection) scores obtained by the PLS-DA models.
231 These scores estimate the importance of each variable in the projection used in the PLS-DA model.
232 A variable with a VIP score close to or higher than 1 can be considered important in a given model.

233 For both the pre-treatments, similar regions with VIP score higher than 1 were obtained, suggesting
234 that the wavelengths with the highest contribution are in the NIR region of the spectrum (from 700
235 to 1000 nm). Consequently, the variable selection method based on the VIP scores higher than 1 was
236 used to reduce the original data set.

237 PLS-DA results (percentage of correctly classified samples) obtained by using the reduced number
238 of variables (wavelengths), are reported in Table 3. In particular, 93 (SNV + MC) and 88
239 (SNV + D1 + MC) x-variables were used to develop the new PLS-DA. The percentages of correctly
240 classified samples are slightly lower (from 86 to 91%) than those obtained considering the whole
241 spectrum. However, the results are still completely acceptable. This confirms also by the high AUC
242 values (0.939 and 0.942).

243 This work presents a solution for in-field and non-destructively determination of grape maturity
244 degree by using HSI combined with linear chemometric techniques. Particularly, the results confirm
245 the suitability for estimating the soluble solid content of red grapes.

246 The positioning of the vineyard row did not create any obstacles regarding the direct solar lighting of
247 the grape bunches. The images along the vineyard row were acquired in the NNE-SSO direction, with
248 the row on the right-hand side of the scanning direction. Consequently, the suitable period for analysis
249 was during the late morning and not later than midday. To scan the other side of the row, it would
250 have been necessary to proceed after midday. Shadows also did not present any problems, as the sun
251 was behind the camera at the time of the acquisitions. To correctly acquire hyperspectral images, the
252 vines should be stripped to ensure that the upper leaves do not overshadow the grapes below. Grapes
253 often had reflection and shaded areas, which need to be excluded during the selection of the ROIs,
254 along with fully or partially shaded grape bunches. In the presence of clouds or even just a slight
255 cloud cover, a significant variation in light intensity was observed: this means that the camera would
256 need to be recalibrated every time a section of the row was scanned. In addition, it is possible that the
257 brightness conditions change soon after calibration, so it would be necessary to recalibrate and
258 immediately proceed with the scan of the row section.

259 The variability grape of a vineyards, in terms of SCC, often is quite high. This depends on many
260 factors, such us the vineyards orientation, unevenness of the land and meteorological phenomena. For
261 this reason, the grapes are harvested at different times even along the same row. Consequently, to
262 optimise the harvest, a technique that allows to have a mapping of the SCC for all grapes, would
263 certainly be an advantage.

264

265 **4. Conclusions**

266 Hyperspectral imaging technology, usually adopted in laboratories with auxiliary artificial lighting,
267 was used in-field under natural lighting conditions to monitor the maturity degree of ‘Sangiovese’
268 (*Vitis vinifera* L.) grapes. The results achieved confirm that it is possible to predict the soluble solid
269 content and to classify grape samples into two classes (not-ripe and ripe) using a linear technique to
270 elaborate the spectral data. Furthermore, the classification performance remained substantially
271 unchanged by reducing the number of wavelengths, so it is expected that a less expensive
272 multispectral camera in the 400–1000 nm range can work just as well. The implementation of a
273 hyperspectral imaging system on an agricultural vehicle coupled to a gimbal stabilisation system,
274 together with the development of hyperspectral image segmentation techniques, would allow
275 on-the-go analysis of large vineyard extensions. Attention should be paid to the presence of water on
276 the surface of the sample under analysis, to the presence of variable cloudiness and, if the leaves are
277 analysed, to the presence of wind.

278

279 **Declarations of interest: none.**

280

281 **References**

282 Acevedo-Opazo, C., Ortega-Farias, S., & Fuentes, S. (2010). Effects of grapevine (*Vitis vinifera* L.)
283 water status on water consumption, vegetative growth and grape quality: An irrigation scheduling

284 application to achieve regulated deficit irrigation. *Agricultural Water Management*, 97(7), 956–964.
285 <https://doi.org/10.1016/j.agwat.2010.01.025>

286

287 Benelli, A., Cevoli, C., & Fabbri, A. (2020). In-field hyperspectral imaging: An overview on the
288 ground-based applications in agriculture. *Journal of Agricultural Engineering*, LI(1030), 129–139.
289 <https://doi.org/10.4081/jae.2020.1030>

290

291 Bucelli, P., Costantini, E. A. C., & Storchi, P. (2010). It is possible to predict sangiovese wine quality
292 through a limited number of variables measured on the vines. *Journal International Des Sciences de*
293 *La Vigne et Du Vin*, 44(4), 207–218. <https://doi.org/10.20870/oeno-one.2010.44.4.1473>

294

295 Camps, C., & Christen, D. (2009). On-tree follow-up of apricot fruit development using a hand-held
296 NIR instrument. *Journal of Food, Agriculture and Environment*, 7(2), 394–400.

297

298 Chandrasekaran, I., Panigrahi, S. S., Ravikanth, L., & Singh, C. B. (2019). Potential of Near-Infrared
299 (NIR) Spectroscopy and Hyperspectral Imaging for Quality and Safety Assessment of Fruits: an
300 Overview. *Food Analytical Methods*, 12(11), 2438–2458. [https://doi.org/10.1007/s12161-019-](https://doi.org/10.1007/s12161-019-01609-1)
301 [01609-1](https://doi.org/10.1007/s12161-019-01609-1)

302

303 Deborah, H., Richard, N., & Hardeberg, J. Y. (2015). A Comprehensive Evaluation of Spectral
304 Distance Functions and Metrics for Hyperspectral Image Processing. *IEEE Journal of Selected Topics*
305 *in Applied Earth Observations and Remote Sensing*, 8(6), 3224–3234.
306 <https://doi.org/10.1109/JSTARS.2015.2403257>

307

308 Deery, D., Jimenez-Berni, J., Jones, H., Sirault, X., & Furbank, R. (2014). Proximal remote sensing
309 buggies and potential applications for field-based phenotyping. *Agronomy*, 4(3), 349–379.
310 <https://doi.org/10.3390/agronomy4030349>
311

312 Delrot, S., Medrano, H., Or, E., Bavaresco, L., & Grando, S. (2010). Preface. In *Methodologies and*
313 *Results in Grapevine Research* (pp. 1–448). Springer Netherlands. <https://doi.org/10.1007/978-90->
314 [481-9283-0](https://doi.org/10.1007/978-90-481-9283-0)
315

316 Diezma-Iglesias, B., Barreiro, P., Blanco, R., & García-Ramos, F. J. (2008). Comparison of robust
317 modeling techniques on NIR spectra used to estimate grape quality. *Acta Horticulturae*, 802, 367–
318 372. <https://doi.org/10.17660/ActaHortic.2008.802.48>
319

320 ElMasry, G., Wang, N., ElSayed, A., & Ngadi, M. (2007). Hyperspectral imaging for nondestructive
321 determination of some quality attributes for strawberry. *Journal of Food Engineering*, 81(1), 98–107.
322 <https://doi.org/10.1016/j.jfoodeng.2006.10.016>
323

324 FAO (Food and Agriculture Organization). (2009). Grapes Wine. In *FAO Agribusiness handbook* (p.
325 49). <http://www.fao.org/3/al176e/al176e.pdf>
326

327 Gallagher, N. B., Shaver, J. M., Martin, E. B., Morris, J., Wise, B. M., & Windig, W. (2004). Curve
328 resolution for multivariate images with applications to TOF-SIMS and Raman. *Chemometrics and*
329 *Intelligent Laboratory Systems*, 73(1 SPEC. ISS.), 105–117.
330 <https://doi.org/10.1016/j.chemolab.2004.04.003>
331

332 Guidetti, R., Beghi, R., & Bodria, L. (2010). Evaluation of grape quality parameters by a simple
333 VIS/NIR system. *Transactions of the ASABE*, 53(2), 477–484.

334

335 Guo, W., Li, W., Yang, B., Zhu, Z. Z., Liu, D., & Zhu, X. (2019). A novel noninvasive and cost-
336 effective handheld detector on soluble solids content of fruits. *Journal of Food Engineering*,
337 257(March), 1–9. <https://doi.org/10.1016/j.jfoodeng.2019.03.022>

338

339 Gutiérrez, S., Fernández-Navales, J., Diago, M. P., & Tardaguila, J. (2018a). On-the-go hyperspectral
340 imaging under field conditions and machine learning for the classification of grapevine varieties.
341 *Frontiers in Plant Science*, 9(July), 1–11. <https://doi.org/10.3389/fpls.2018.01102>

342

343 Gutiérrez, S., Tardaguila, J., Fernández-Navales, J., & Diago, M. P. (2018b). On-the-go hyperspectral
344 imaging for the in-field estimation of grape berry soluble solids and anthocyanin concentration.
345 *Australian Journal of Grape and Wine Research*, i, 127–133. <https://doi.org/10.1111/ajgw.12376>

346

347 Huang, Y., Lee, M. A., Thomson, S. J., & Reddy, K. N. (2016). Ground-based hyperspectral remote
348 sensing for weed management in crop production. *International Journal of Agricultural and*
349 *Biological Engineering*, 9(2), 98–109. <https://doi.org/10.3965/j.ijabe.20160902.2137>

350

351 Ishida, T., Kurihara, J., Viray, F. A., Namuco, S. B., Paringit, E. C., Perez, G. J., Takahashi, Y., &
352 Marciano, J. J. (2018). A novel approach for vegetation classification using UAV-based hyperspectral
353 imaging. *Computers and Electronics in Agriculture*, 144(December 2017), 80–85.
354 <https://doi.org/10.1016/j.compag.2017.11.027>

355

356 Jay, S., Gorretta, N., Morel, J., Maupas, F., Bendoula, R., Rabatel, G., Dutartre, D., Comar, A., &
357 Baret, F. (2017). Estimating leaf chlorophyll content in sugar beet canopies using millimeter- to
358 centimeter-scale reflectance imagery. *Remote Sensing of Environment*, 198, 173–186.
359 <https://doi.org/10.1016/j.rse.2017.06.008>

360

361 Liu, D., Zeng, X. A., & Sun, D. W. (2015). Recent Developments and Applications of Hyperspectral
362 Imaging for Quality Evaluation of Agricultural Products: A Review. *Critical Reviews in Food Science
363 and Nutrition*, 55(12), 1744–1757. <https://doi.org/10.1080/10408398.2013.777020>

364

365 Manley, M., Joubert, E., Myburgh, L., & Kidd, M. (2007). Prediction of soluble solids content and
366 post-storage internal quality of Bulida apricots using near infrared spectroscopy. *Journal of Near
367 Infrared Spectroscopy*, 15(3), 179–188. <https://doi.org/10.1255/jnirs.725>

368

369 Matese, A., & Di Gennaro, S. F. (2015). Technology in precision viticulture: A state of the art review.
370 *International Journal of Wine Research*, 7(1), 69–81. <https://doi.org/10.2147/IJWR.S69405>

371

372 McGlone, V. A., & Kawano, S. (1998). Firmness, dry-matter and soluble-solids assessment of
373 postharvest kiwifruit by NIR spectroscopy. *Postharvest Biology and Technology*, 13(2), 131–141.
374 [https://doi.org/10.1016/S0925-5214\(98\)00007-6](https://doi.org/10.1016/S0925-5214(98)00007-6)

375

376 Munera, S., Besada, C., Blasco, J., Cubero, S., Salvador, A., Talens, P., & Aleixos, N. (2017).
377 Astringency assessment of persimmon by hyperspectral imaging. *Postharvest Biology and
378 Technology*, 125, 35–41. <https://doi.org/10.1016/j.postharvbio.2016.11.006>

379

380 Nicolaï, B. M., Beullens, K., Bobelyn, E., Peirs, A., Saeys, W., Theron, K. I., & Lammertyn, J. (2007).
381 Nondestructive measurement of fruit and vegetable quality by means of NIR spectroscopy: A review.
382 *Postharvest Biology and Technology*, 46(2), 99–118.
383 <https://doi.org/10.1016/j.postharvbio.2007.06.024>

384

385 OIV (International Organisation of Vine and Wine). (2019). *2019 Statistical Report on World*
386 *Vitiviniculture* (p. 23). <https://doi.org/64/19/6835> [pii]\n10.1158/0008-5472.CAN-04-1678
387

388 Pellegrino, A., Lebon, E., Simonneau, T., & Wery, J. (2005). Towards a simple indicator of water
389 stress in grapevine (*Vitis vinifera* L.) based on the differential sensitivities of vegetative growth
390 components. *Australian Journal of Grape and Wine Research*, *11*(3), 306–315.
391 <https://doi.org/10.1111/j.1755-0238.2005.tb00030.x>
392

393 Pu, H., Liu, D., Wang, L., & Sun, D. W. (2016). Soluble Solids Content and pH Prediction and
394 Maturity Discrimination of Lychee Fruits Using Visible and Near Infrared Hyperspectral Imaging.
395 *Food Analytical Methods*, *9*(1), 235–244. <https://doi.org/10.1007/s12161-015-0186-7>
396

397 Rinnan, Å., van den Berg, F., & Engelsen, S. B. (2009). Review of the most common pre-processing
398 techniques for near-infrared spectra. *TrAC Trends in Analytical Chemistry*, *28*(10), 1201–1222.
399 <https://doi.org/10.1016/J.TRAC.2009.07.007>
400

401 Teixeira Dos Santos, C. A., Lopo, M., Páscoa, R. N. M. J., & Lopes, J. A. (2013). A review on the
402 applications of portable near-infrared spectrometers in the agro-food industry. *Applied Spectroscopy*,
403 *67*(11), 1215–1233. <https://doi.org/10.1366/13-07228>
404

405 Underwood, J., Wendel, A., Schofield, B., McMurray, L., & Kimber, R. (2017). Efficient in-field
406 plant phenomics for row-crops with an autonomous ground vehicle. *Journal of Field Robotics*, *34*(6),
407 1061–1083. <https://doi.org/10.1002/rob.21728>
408

409 Wendel, A., Underwood, J., & Walsh, K. (2018). Maturity estimation of mangoes using hyperspectral
410 imaging from a ground based mobile platform. *Computers and Electronics in Agriculture*, 155(June),
411 298–313. <https://doi.org/10.1016/j.compag.2018.10.021>

412

413 Whetton, R. L., Waine, T. W., & Mouazen, A. M. (2018). Hyperspectral measurements of yellow
414 rust and fusarium head blight in cereal crops: Part 2: On-line field measurement. *Biosystems
415 Engineering*, 167, 144–158. <https://doi.org/10.1016/j.biosystemseng.2018.01.004>

416

417 Zarco-Tejada, P. J., Guillén-Climent, M. L., Hernández-Clemente, R., Catalina, A., González, M. R.,
418 & Martín, P. (2013). Estimating leaf carotenoid content in vineyards using high resolution
419 hyperspectral imagery acquired from an unmanned aerial vehicle (UAV). *Agricultural and Forest
420 Meteorology*, 171–172, 281–294. <https://doi.org/10.1016/j.agrformet.2012.12.013>

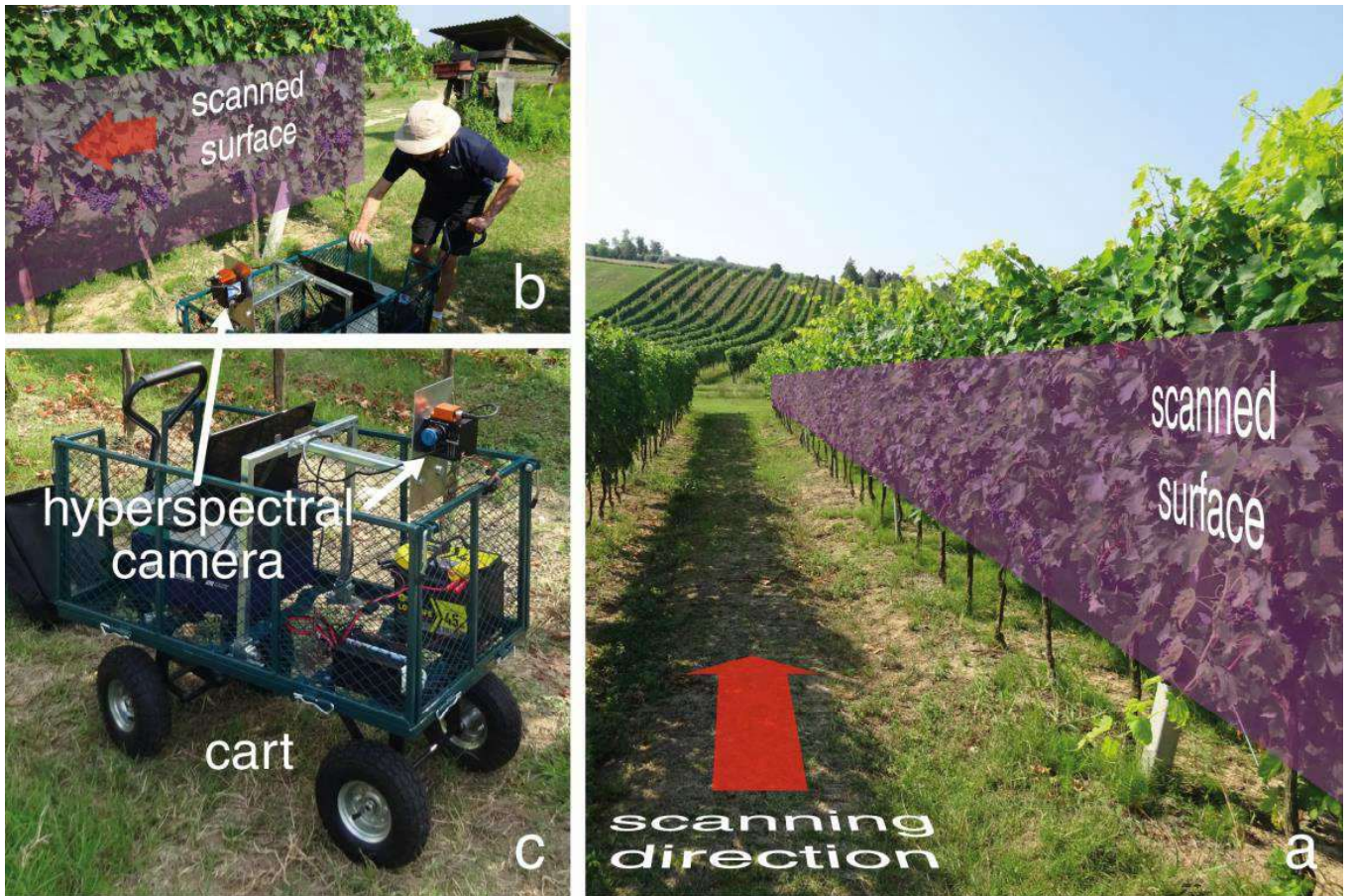


Fig.1

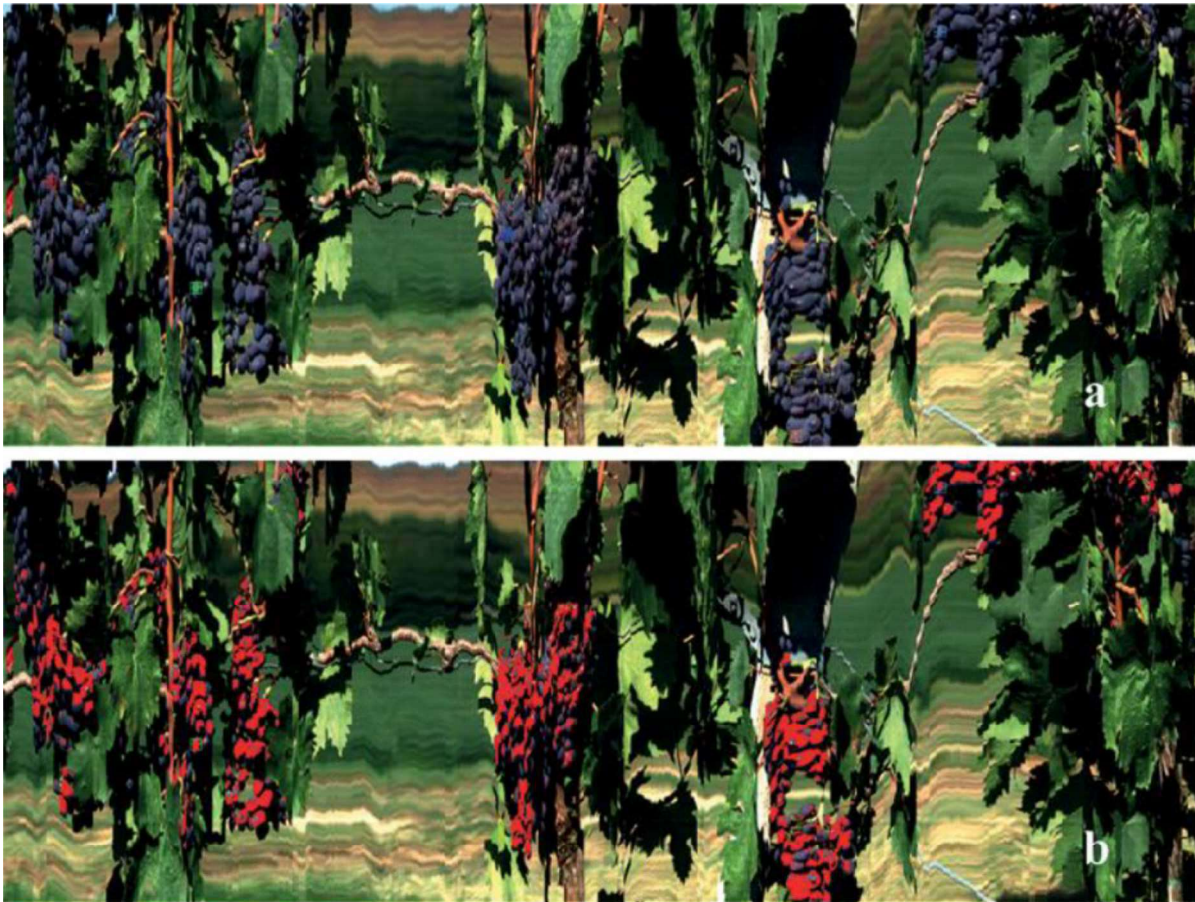


Fig. 2

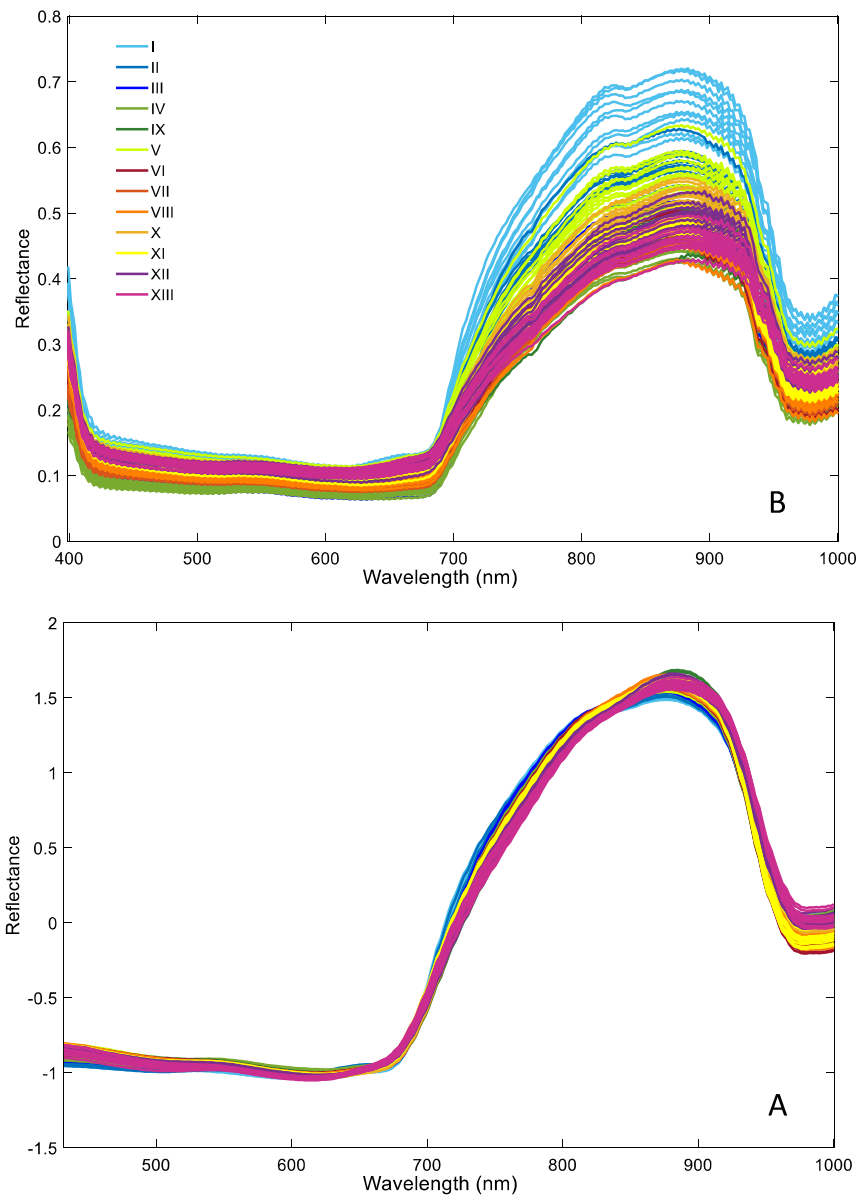


Fig. 3

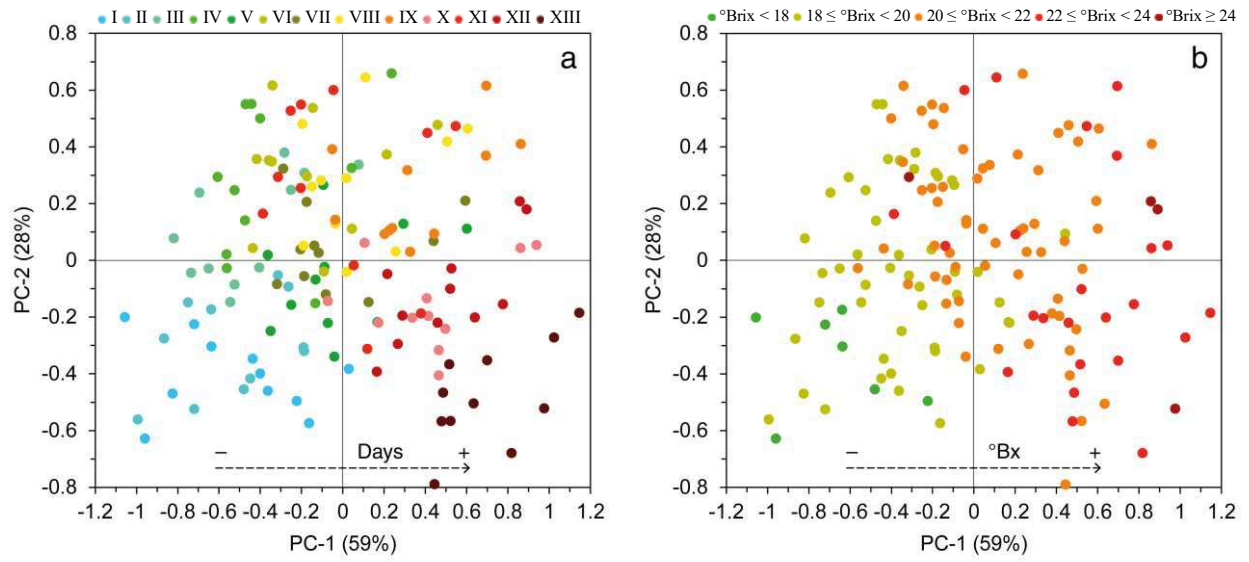


Fig. 4

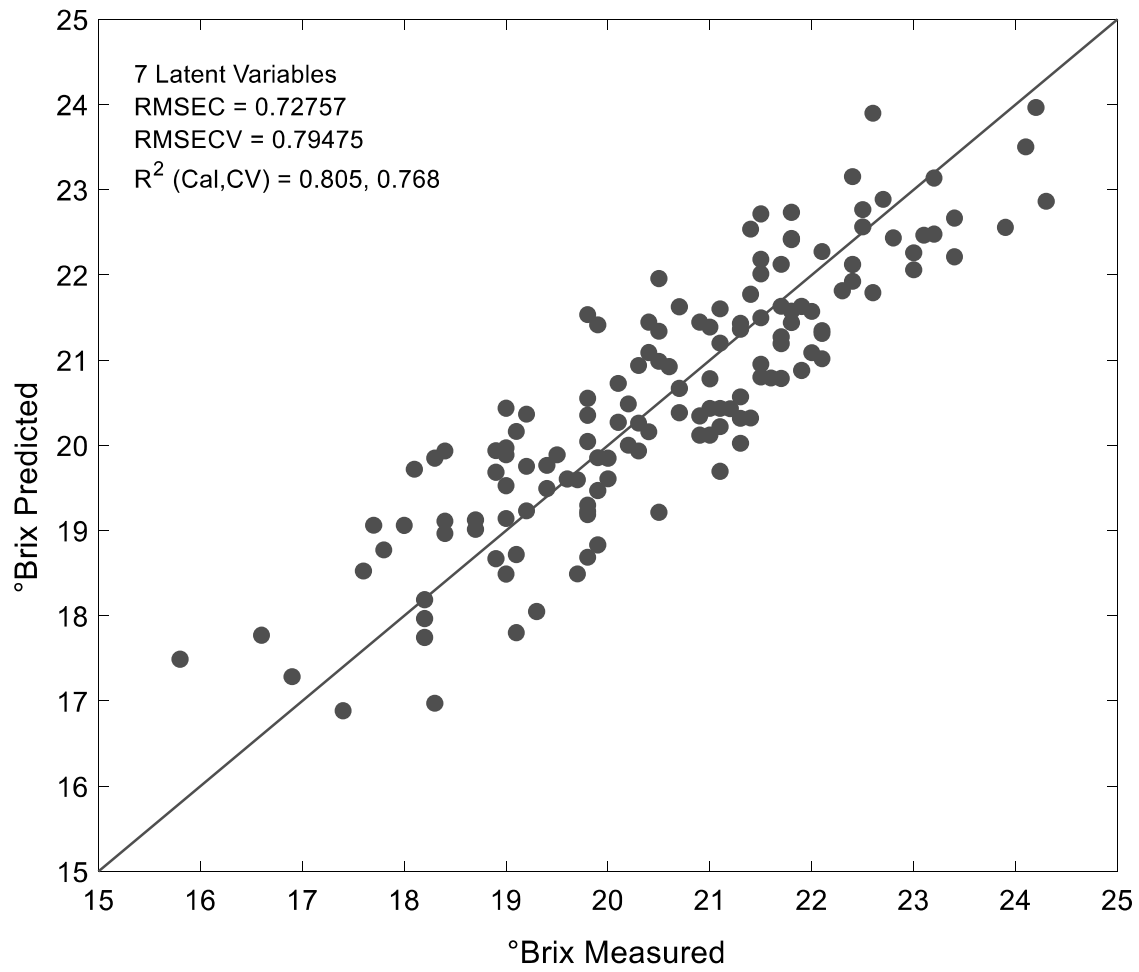


Fig. 5

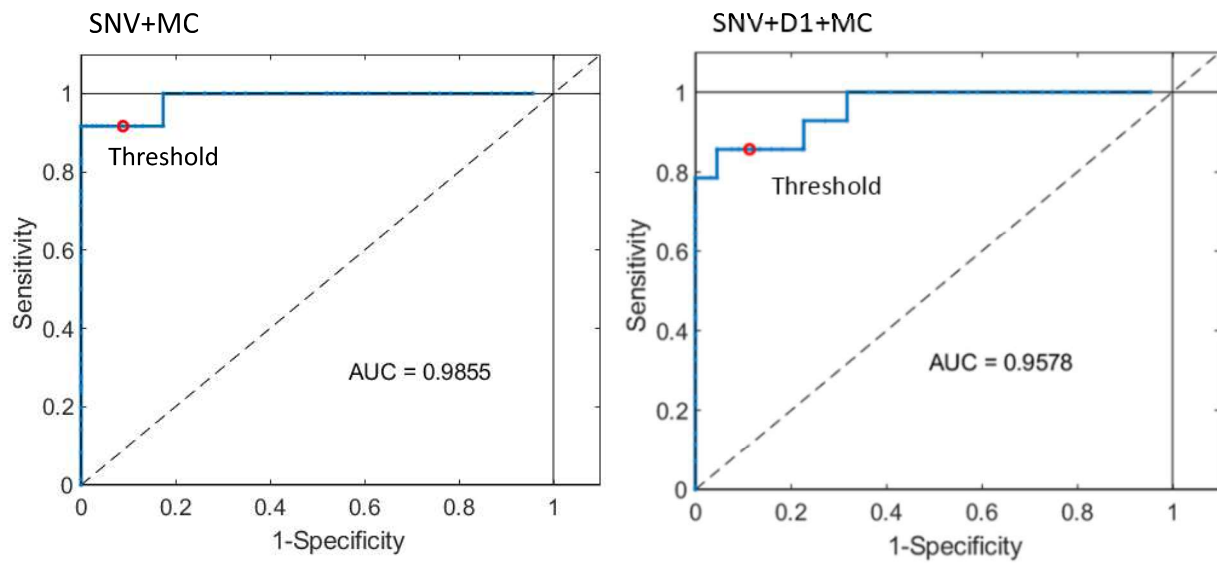


Fig. 6

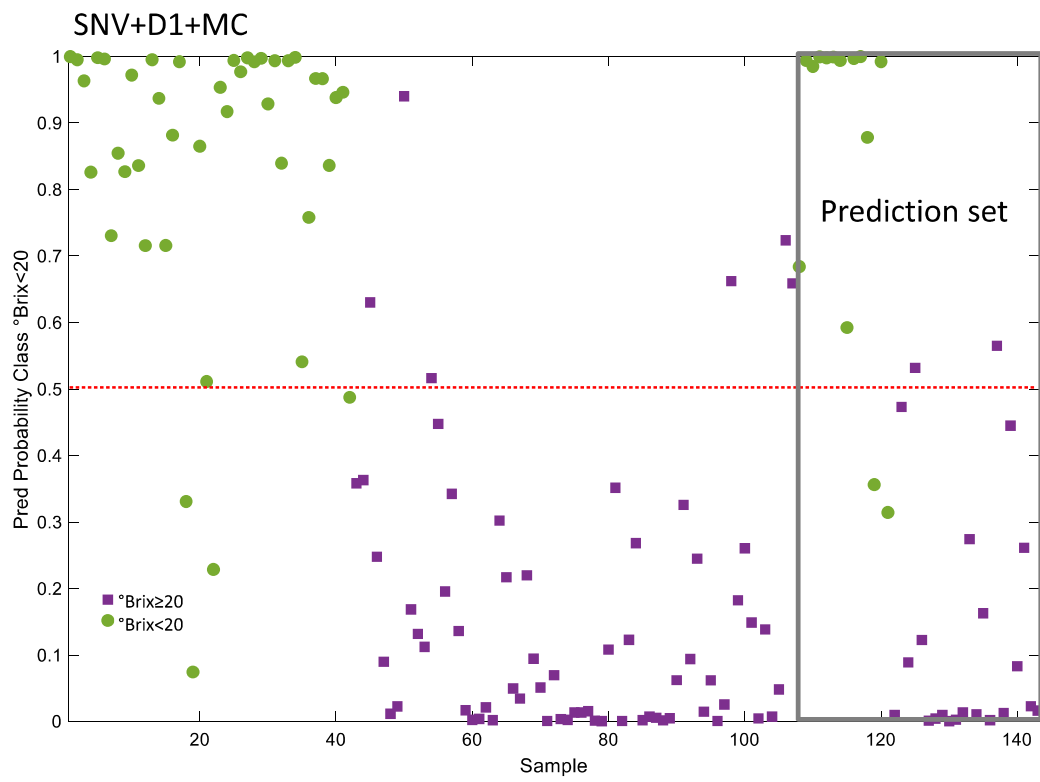
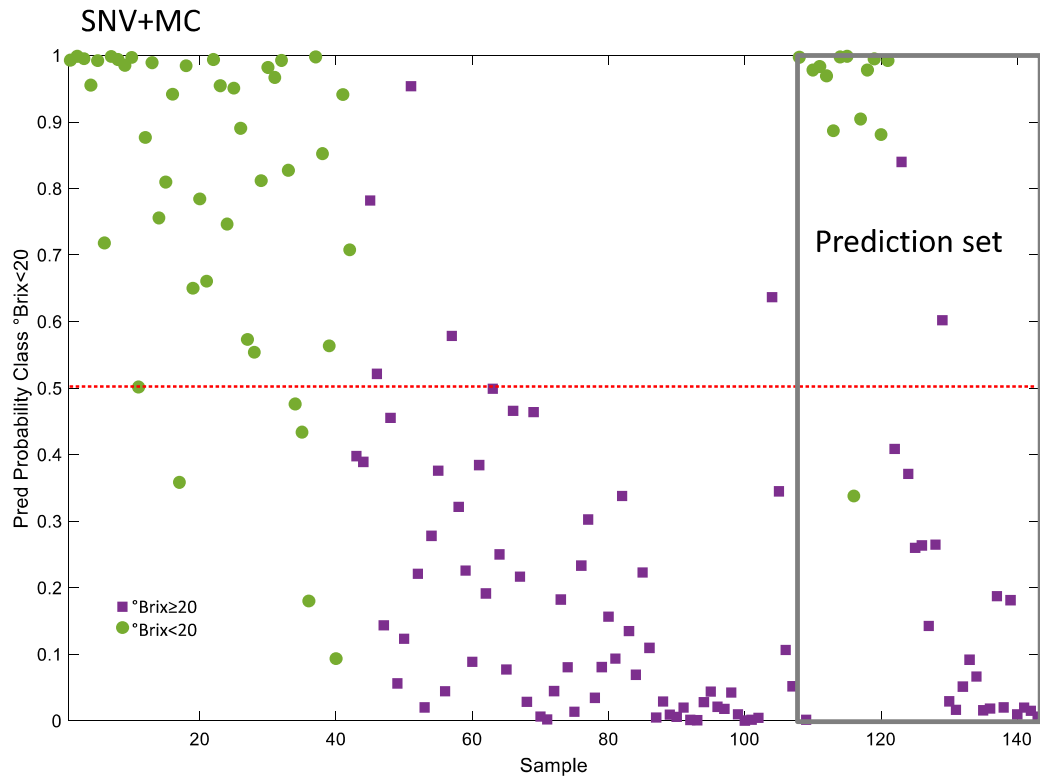


Fig. 7

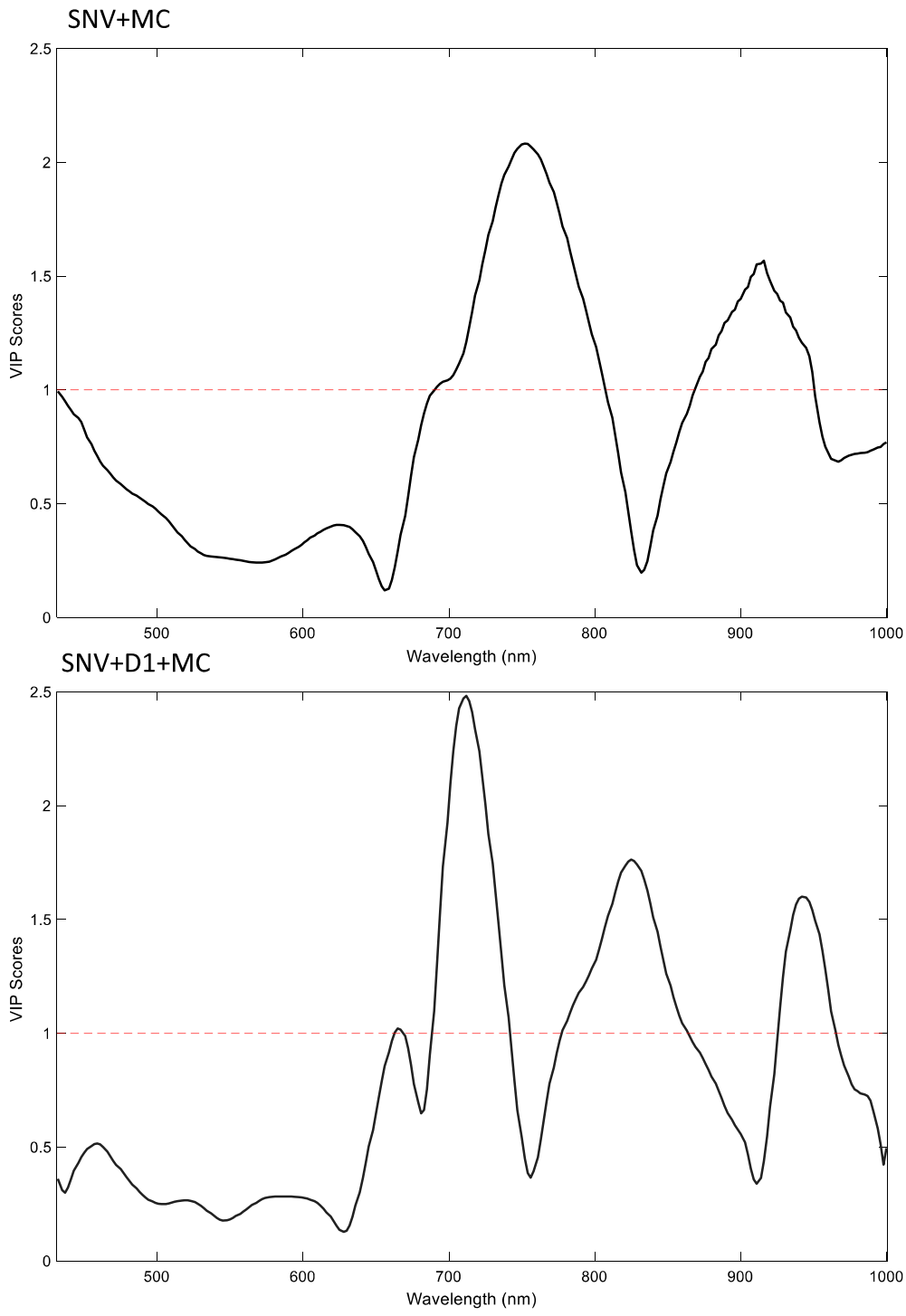


Fig. 8

1 **Figure captions**

2 **Fig. 1.** (a) Vineyard row, highlighted by the purple surface, scanned with the Vis/NIR hyperspectral
3 camera; red arrow indicates the direction of scanning; (b) Garden cart mounted with hyperspectral
4 camera. (c) In-field hyperspectral imaging to measure soluble solids content of wine grape berries
5 during ripening.

6 **Fig. 2.** (a) RGB image from hyperspectral image of a scanned vineyard row section. (b)
7 Representation of the ROI (in red) resulting from the classification obtained by the Manhattan
8 function.

9 **Fig. 3.** Raw (A) and pre-treated by smoothing and SNV (B) spectra of all samples on different days
10 of analysis (from I to XIII).

11 **Fig. 4.** Score plot obtained by the PCA according to: (a) days of analysis (from I to XIII); (b) soluble
12 solids content ($^{\circ}$ Brix).

13 **Fig. 5.** Measured vs predicted values of solid soluble content ($^{\circ}$ Brix) obtained by PLS regression
14 (cross validation).

15 **Fig. 6.** ROC curve of the PLS-DA models in prediction.

16 **Fig. 7.** Probability values of belonging to the class $^{\circ}$ Brix<20.

17 **Fig. 8.** VIP scores of the PLS-DA.

Table 1. Mean and standard deviation values of soluble solids content (°Brix) as a function of days of analysis.

| Day of analysis | Mean (°Brix) | Standard deviation (°Brix) |
|-----------------|-------------------------|----------------------------|
| I | 17.8 ^a | 1.05 |
| II | 19.0 ^{a,b} | 0.81 |
| III | 19.2 ^{b,c} | 0.75 |
| IV | 19.9 ^{b,c,d} | 1.1 |
| V | 20.1 ^{b,c,d} | 1.16 |
| VI | 20.2 ^{b,c,d,e} | 0.95 |
| VII | 20.5 ^{c,d,e,f} | 1.11 |
| VIII | 20.7 ^{d,e,f} | 0.82 |
| IX | 21.5 ^{e,f,g} | 0.76 |
| X | 21.6 ^{e,f,g} | 0.89 |
| XI | 21.7 ^{f,g} | 1.17 |
| XII | 22.7 ^g | 0.94 |
| XIII | 22.7 ^g | 0.88 |

Note: means with the same letter are not significant different at p-level < 0.05.

Table 2. PLS-DA results in terms of percentages of correctly classified samples (whole spectral range).

| Spectra pretreatment | Class | Calibration (n=107) | Cross-validation (n=107, 10 segments) | Prediction (n=36) | LV |
|----------------------|----------|------------------------|--|----------------------|----|
| SNV+MC | °Brix<20 | 89% | 89% | 91% | 4 |
| | °Brix≥20 | 91% | 91% | 91% | |
| SNV+D1+ MC | °Brix<20 | 91% | 89% | 86% | 4 |
| | °Brix≥20 | 91% | 91% | 91% | |

Note: SNV=Standard Normal Variate; MC=Mean Cantered; D1=first derivative, LV=Latent Variable.

Table 3. PLS-DA results in terms of percentages of correctly classified samples (reduced spectral range).

| Spectra pretreatment | Class | Calibration (n=107) | Cross-validation (n=107, 10 segments) | Prediction (n=36) | LV |
|----------------------|----------|------------------------|--|----------------------|----|
| SNV+MC | °Brix<20 | 84% | 83% | 86% | 4 |
| | °Brix≥20 | 93% | 92% | 91% | |
| SNV+D1+ MC | °Brix<20 | 89% | 89% | 88% | 3 |
| | °Brix≥20 | 90% | 87% | 87% | |

Note: SNV=Standard Normal Variate; MC=Mean Centered; D1=first derivative, LV=Latent Variable.

Nomenclature

| | |
|--------|---|
| AUC | area under the curve |
| CV | cross validation |
| D1 | first derivative |
| HSI | hyperspectral imaging |
| MC | mean centring |
| NIR | near-infrared |
| PCA | principal component analysis |
| PLS | partial least squares |
| PLS-DA | partial least squares discriminant analysis |
| R | reflectance spectrum |
| RMSE | root mean square error |
| ROC | receiver operating characteristic |
| ROI | region of interest |
| SNV | standard normal variate |
| SSC | soluble solids content |
| SVM | support vector machines |
| VIP | variable importance in projection |

Declaration of interests

The authors declare that they have no known competing financial interests or personal relationships that could have appeared to influence the work reported in this paper.

The authors declare the following financial interests/personal relationships which may be considered as potential competing interests: